Boosting CO_2 hydrogenation performance for light olefin synthesis over $GaZrO_x$ combined with SAPO-34

Peng Zhang [1], Lixuan Ma [1], Fanhui Meng [*], Lina Wang, Riguang Zhang [*], Guinan Yang, Zhong Li [*]

State Key Laboratory of Clean and Efficient Coal Utilization, Taiyuan University of Technology, Taiyuan, 030024 Shanxi, PR China

ABSTRACT

A highly active and selective $GaZrO_x$/SAPO-34 bifunctional catalyst was developed for CO_2 hydrogenation into $C_2^=$–$C_4^=$. A high $C_2^=$–$C_4^=$ selectivity of 88.8% at CO_2 conversion of 26.7% was achieved, and the olefin yield reached 11.3%, outperforming the previous reports. As Ga:Zr atomic ratio increases, the surface oxygen vacancy content (O_V), responsible for CO_2 activation, firstly increases from 22.5% to 32.6% and then decreases to 15.4%, while the H_2 dissociation ability produced by Ga site increases gradually. Activated CO_2 at Zr–O_V–Zr site could either react with Ga–$H^{\delta-}$ to form HCOO* , then successive hydrogenation to CH_3O* intermediate, or combine with O–$H^{\delta+}$ to form COOH* , followed by dissociation to form CO. The formation of CH_3O* or CO is competitive, which highly depends on the H_2 dissociation ability, only the moderate H_2 dissociation ability benefits CO_2 hydrogenation to CH_3O* at high temperature, leading to a high $C_2^=$–$C_4^=$ yield.

1. Introduction

The utilization of CO_2 to synthesize light olefin ($C_2^=$–$C_4^=$), the crucial raw material in chemical industry, has attracted great attentions in recent years [1,2], which could not only mitigate the climate change caused by CO_2 emission, but also provide a new sustainable synthesis route to reduce the consumption of fossil fuels [3]. By employing Fe-based catalysts, CO_2 is firstly converted to CO via reverse water gas shift (RWGS) reaction, followed by hydrogenation of CO to $C_2^=$–$C_4^=$ via Fischer-Tropsch to olefin synthesis route (FTO) [4,5], but, the selectivity of $C_2^=$–$C_4^=$ hardly exceed 60%, which is limited by the Anderson–Schulz–Flory (ASF) rule [6].

Recently, bifunctional catalysts composed of metal oxide and zeolite are employed to catalyze CO_2 hydrogenation into $C_2^=$–$C_4^=$ with high selectivity of ~80% in the hydrocarbon products [1,7–9]. In this catalytic route, the hydrogenation of CO_2 occurs on the surface of metal oxide to form CH_xO (CH_3O*, CH_3OH) intermediate, and then converts into $C_2^=$–$C_4^=$ by the zeolite's acidic sites. The C–C coupling of CH_xO over zeolite requires the reaction temperature of about 400 °C [10], however, such high reaction temperature results in the formation of CO via RWGS reaction as the dominant product rather than the CH_xO intermediate over metal oxide [9]. As a result, reducing the selectivity of total

hydrocarbon products, the obtained yield of $C_2^=$–$C_4^=$ was normally less than 7% [11–16]. For example, by employing Zn-Zr/SAPO-34 catalyst [11], the $C_2^=$–$C_4^=$ selectivity reached as high as 80% in hydrocarbon products at CO_2 conversion of 18% (400 °C, 2.0 MPa), but the CO selectivity was 65%, leading to the low $C_2^=$–$C_4^=$ yield of 5.0%. By employing In-Zr /SAPO-34 catalyst [13], the CO_2 conversion reached as high as 35.5%, and the $C_2^=$–$C_4^=$ selectivity was 76.4% (400 °C, 3.0 MPa), but the $C_2^=$–$C_4^=$ yield was only 5.4%. The reason is that the most of CO_2 converts to CO, about 80%, and only 7.1% to hydrocarbons. Since the higher CO_2 conversion is always along with the higher CO selectivity, it is necessary, albeit very challenging, to develop the novel metal oxide catalyst to boost the selective conversion of CO_2 to CH_xO instead of CO at high temperature, and further enhance the $C_2^=$–$C_4^=$ yield after combined with SAPO-34 zeolite.

Extensive studies have revealed that the oxygen vacancy on the metal oxide surface benefits the CO_2 adsorption, activation and to form CH_3OH intermediates [17–20]. Liu et al. reported that over the $ZnGa_2O_4$ catalyst, the increase of density of oxygen vacancy linearly enhanced the formation rates of methanol/dimethyl ether [15]. Density functional theory (DFT) calculations revealed that the oxygen vacancy created by incorporation of Zr to In_2O_3 surface facilitates to form and stabilize CH_3OH while strongly suppress the CO formation [13]. It is indicated

that abundant and special oxygen vacancy of metal oxides is essential to boost the conversion of CO_2 to CH_xO, consequently to increase the $C_2^=$–$C_4^=$ yield. It is well known that ZrO_2 surface easily produce sufficient oxygen vacancy to activate CO_2 [21–25], but it has a little H_2 activation ability [26]. Therefore, adding another component with hydrogen dissociation ability to ZrO_2 is essential for CO_2 hydrogenation to CH_xO such as ZnO [27], In_2O_3 [24], CdO [19]. In addition to these oxides, Ga_2O_3 has the similar property to activate the H_2 with heterolytic dissociation [28,29]. Pan et al. found that high temperature facilitates the H_2 dissociation on Ga_2O_3 and produce GaH species [29]. Our recent work found that Ga_2O_3 provides a proper H_2 dissociation ability to boost the conversion of syngas into light olefin by employing Ga-Mn oxide/SAPO-34 [30]. Witoon et al. reported that the adding Ga to In_2O_3 benefits the CO_2 hydrogenation to methanol and suppress the RWGS reaction at high temperature [18]. It is suggested that $GaZrO_x$ with SAPO-34 perhaps have an excellent catalytic activity and selectivity to synthesize $C_2^=$–$C_4^=$ from CO_2 hydrogenation. To the best of our knowledge, there has been no research reports on this catalyst and the synergistic effect of Zr and Ga on CO_2 hydrogenation to $C_2^=$–$C_4^=$ is unclear.

In this work, the binary $GaZrO_x$ with SAPO-34 catalyst for CO_2 hydrogenation into $C_2^=$–$C_4^=$ was investigated. The structure, physicochemical properties, and electronic properties of $GaZrO_x$ with different Ga:Zr atomic ratios were characterized to reveal the relationship between the structure and activity. The CO_2/H_2 adsorption, activation, and the hydrogenation mechanism were discussed.

2. Experimental section

2.1. Catalytic preparation

A series of $GaZrO_x$ with different Ga:Zr atomic ratios (1:16, 1:8, 1:4, 4:1) as well as the sole ZrO_2, Ga_2O_3 were prepared via parallel flow co-precipitation method. Typically, the required amount of $Zr(NO_3)_2 \cdot 5H_2O$ and $Ga(NO_3)_2 \cdot 9H_2O$ were dissolved in deionized water to form a mixed salt solution with total concentration of Ga and Zr for 1.0 $mol \cdot L^{-1}$. An aqueous solution of ammonia (1.0 $mol \cdot L^{-1}$) was prepared as the precipitation agent. Then they were simultaneously added dropwise to 100 mL deionized water under continuous stirring at 30 ℃. The pH value of the aqueous solution was kept at 7.0 ± 0.1 by adjusting the addition rate of the basic solution, the obtained suspension was aged for 1 h at 60 ℃, and then centrifuged, washed with deionized water until neutral. Finally, the precipitate was dried at 110 ℃ for 12 h, and calcined in air at 450 ℃ for 4 h. The obtained samples for $GaZrO_x$ with various Ga:Zr atomic ratios were named as Ga:Zr(m:n), where m:n is the atomic ratio of Ga:Zr.

SAPO-34 zeolite was hydrothermally synthesized as presented in our previous reports [30]. More information about the SAPO-34 preparation is given in Supporting information (SI).

Bifunctional catalyst was prepared by mortar-mixing configuration, in which the SAPO-34 and $GaZrO_x$ oxides with a mass ratio of 1:2 were grounded in an agate mortar for 10 min to mix well, and then pressed and crushed into 20–40 mesh particles.

2.2. Catalyst characterization

The samples were characterized by X-ray diffraction (XRD); Raman spectra; Time-of-flight secondary ion mass spectrometry (TOF-SIMS); X-ray photoelectron spectroscopy (XPS); Electron paramagnetic resonance (EPR); Temperature-programmed desorption of CO_2 (CO_2-TPD); Transmission electron microscopy (TEM) and EDX mapping; *In-situ* diffuse reflection infrared Fourier transform (in-situ DRIFT). More information about the catalyst characterization is given in **SI**.

2.3. DFT calculations

Spin-polarized density functional theory (DFT) calculations were implemented by the Vienna Ab Initio Simulation Package (VASP) code [31,32], and the projector augmented wave (PAW) method have been employed. Details are presented in **SI**.

2.4. Catalytic activity test

The reaction of direct hydrogenation of CO_2 into $C_2^=$–$C_4^=$ was tested on a high-pressure fixed-bed reactor. Typically, 0.4 g of bifunctional catalyst was loaded in the quartz tube with inner diameter of 6.0 mm embedded in stainless steel tubular reactor. Prior to reaction, the catalyst was pretreated in the H_2 flow (20 $mL \cdot min^{-1}$) for 4 h at 390 ℃, and then the mixed gas (CO_2/H_2/N_2 = 24:72:4) was introduced. The reaction was carried out under 390 ℃, 3.0 MPa, and 3000 $mL \cdot h^{-1} \cdot g^{-1}$ unless otherwise stated. N_2 was used as an internal standard gas to ensure an accurate carbon balance. Details about the products analysis are presented in **SI**.

3. Results and discussion

3.1. Catalytic activity evaluation

The methanol synthesis (CO_2 + 3 H_2 → CH_3OH + H_2O ΔH^0_{298} = −45.9 $kJ \cdot mol^{-1}$) and RWGS reaction (CO_2 + H_2 → CO + H_2O ΔH^0_{298} = 42.1 $kJ \cdot mol^{-1}$) usually occur simultaneously, whereas the latter is more competitive at high temperature, according to the equilibrium calculations, the equilibrium selectivity of CO reaches 99.3% at 390 ℃, 3.0 MPa (Fig. S1a), compared with the methanol synthesis reaction, the hydrogenation of CO_2 into $C_2^=$–$C_4^=$ is thermodynamically more favorable, the equilibrium selectivity and yield of olefin (represented by ethylene) is 94.0% and 55.5% at 390 ℃, 3.0 MPa (Fig. S1b). It means combining methanol synthesis reaction with MTO reaction can decrease the selectivity of CO and promote $C_2^=$–$C_4^=$ formation. Fig. 1 shows the performance of CO_2 hydrogenation into $C_2^=$–$C_4^=$ over bifunctional catalysts. The effect of different Ga:Zr atomic ratios on catalytic performance is displayed in Fig. 1a, the sole ZrO_2 combined with SAPO-34 shows a high $C_2^=$–$C_4^=$ selectivity of 82.4% in hydrocarbon, but the obtained yield of $C_2^=$–$C_4^=$ is only 0.2%, which is due to the low CO_2 conversion of 9.6% and high CO selectivity of 97%. A small amount of Ga (Ga:Zr=1:16) significantly enhances the CO_2 conversion and $C_2^=$–$C_4^=$ yield, further increasing Ga:Zr atomic ratio, the volcano-type curves are obtained; Meanwhile, the CO selectivity, which produced from RWGS reaction, exhibits an inverted volcanic result as compared with CO_2 conversion and $C_2^=$–$C_4^=$ yield. $GaZrO_x$ with the Ga:Zr atomic ratio of 1:4 shows the highest CO_2 conversion of 26.7% and high $C_2^=$–$C_4^=$ selectivity of 88.8% in hydrocarbon. Moreover, the CO selectivity decreases to the minimum value of 52.4% at the same time, suggesting the introduction of optimized Ga to ZrO_2 not only improve the CO_2 conversion, but also obviously inhibit the CO formation, the obtained $C_2^=$–$C_4^=$ yield is as high as 11.3%, which outperforms the previously reported results as shown in Table S1. Moreover, it is found that the selectivity of $C_2^=$–$C_4^=$ obviously decreases to 75.9% as Ga:Zr ratio reaches 4:1, suggesting that the high content of Ga leads to excessive hydrogenation of light olefin. The catalytic performance can be further enhanced by adjusting the reaction conditions. Fig. 1b and Fig. 1c show that as the temperature increases or GHSV decreases, both CO_2 conversion and $C_2^=$–$C_4^=$ yield gradually boost, while the $C_2^=$–$C_4^=$ selectivity slightly reduces. However, both the reaction temperature and GHSV show little effect on CO selectivity, even at high temperature of 400 ℃ or 410 ℃, the CO selectivity keep about 52–54%. As comparison, for other typically bifunctional catalysts reported in the previous literature, such high reaction temperature leads to the very high CO selectivity of 65–85% (Table S1). The catalytic stability result for Ga:Zr(1:4)/ SAPO-34 catalyst is shown in Fig. 1d. After the induction period, the CO_2

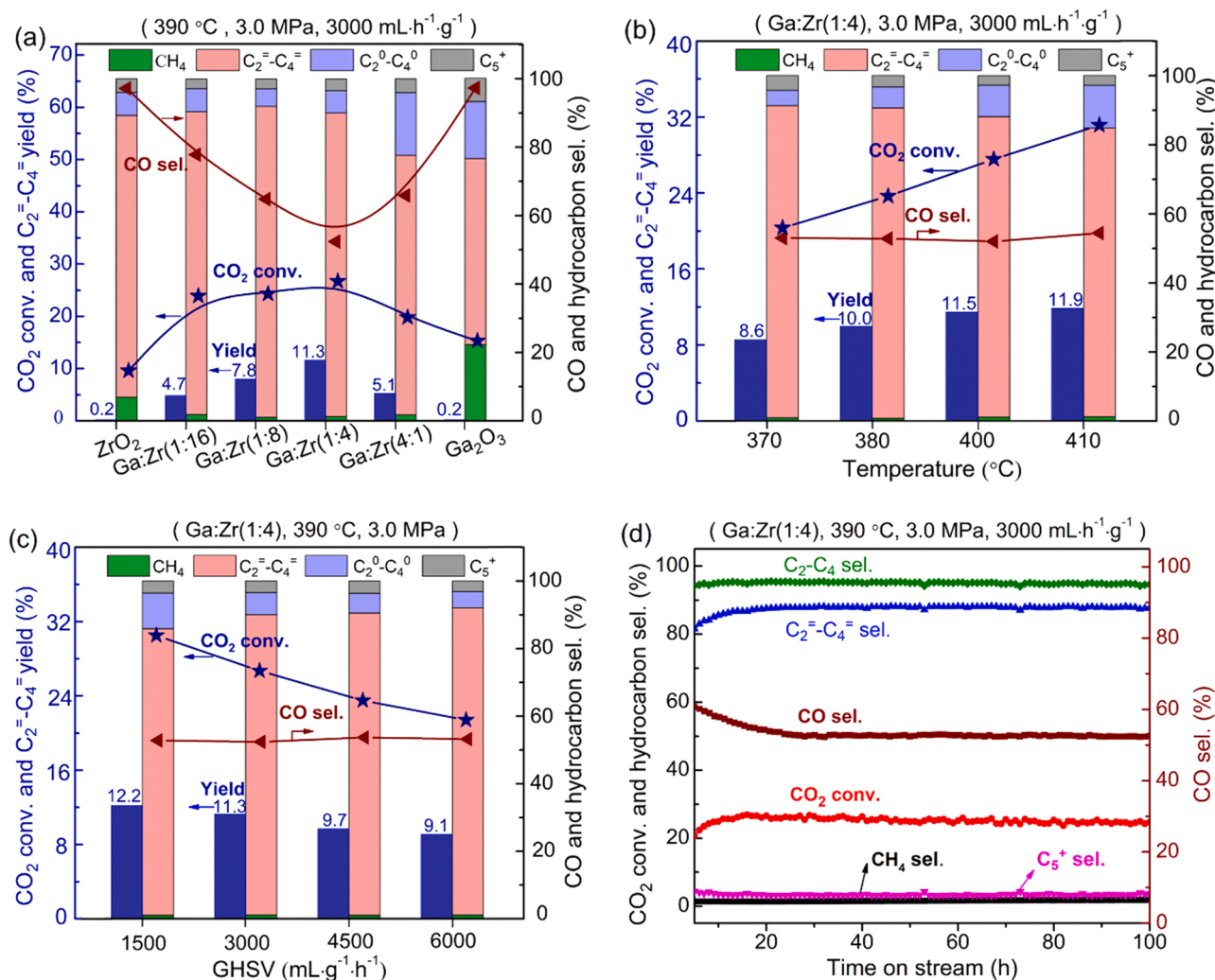**Fig. 1.** Catalytic performance of CO_2 hydrogenation into light olefin over $GaZrO_x$ combined with SAPO-34.

conversion, $C_2^=$–$C_4^=$ selectivity and CO selectivity kept stable at around 26%, 88% and 52%, respectively. No obvious deactivation is observed after a reaction time for 100 h, suggesting a potential for industrial application.

3.2. Structure and morphology analysis

To investigate the structure of $GaZrO_x$ with various Ga:Zr atomic ratios, XRD patterns are performed and displayed in Fig. 2a. The sole ZrO_2 shows the characteristic diffraction peaks at 2θ of 30.3°, 35.3°, 50.6°, 60.2°, 63.0°, and 74.5°, corresponding to tetragonal ZrO_2 (t-ZrO_2, PDF#50–1089), and the very weak diffraction peaks at 24.0°, 28.2°, 31.4° and 40.7° are attributed to monoclinic ZrO_2 (m-ZrO_2, PDF#37–1484). After the introduction of small amount of Ga, the diffraction peaks corresponding to m-ZrO_2 disappear, and the t-ZrO_2 phase of Ga:Zr(1:16) and Ga:Zr(1:8) shifts to higher angles, compared with the sole ZrO_2 as shown in Fig. S3; Moreover, no crystalline phase corresponding to Ga_2O_3 is detected. The results confirm that Ga incorporated into ZrO_2 crystal lattice and thus shrank the ZrO_2 crystal spacing, which is attributed to the larger atomic radius of Zr^{4+}(0.072 nm) than that of Ga^{3+}(0.062 nm). It is interesting to find that Ga:Zr(1:4) exhibits amorphous structure, suggesting that the introduction of certain amount of Ga into ZrO_2 form a highly dispersed Zr and Ga species. Ga:Zr(4:1) exhibits the characteristic peaks of α-Ga_2O_3 (PDF#06–0503), which is similar to that of sole Ga_2O_3. No crystalline phase corresponding to t-ZrO_2 or m-ZrO_2 is detected.

Raman spectra of metal oxides are shown in Fig. 2b. For sole ZrO_2, the characteristic peaks correspond ing to t-ZrO_2 at 148, 268, 316, 461, and 644 cm^{-1} as well as corresponding to m-ZrO_2 at 178, 189, and 382 cm^{-1} are presented, indicating that t-ZrO_2 and m-ZrO_2 are co-existed in sole ZrO_2 sample, and t-ZrO_2 is the dominant phase [33]. For binary oxides Ga:Zr(1:16) and Ga:Zr(1:8), the peaks belonging to m-ZrO_2 disappear, and the peaks intensity for t-ZrO_2 decrease as the Ga:Zr atomic ratio increases. Interestingly, Ga:Zr(1:4) displays no obvious peaks, suggesting the high dispersion of Zr and Ga species in $GaZrO_x$. Further increasing the Ga:Zr atomic ratio, the characteristic peaks corresponding to α-Ga_2O_3 at 218, 287, 433, 570, 648, and 709 cm^{-1} are observed [34], similar to that of sole Ga_2O_3 sample. These results are consistent with XRD analysis.

The molecular specificity and surface sensitivity TOF-SIMS is used to further determine to molecular structure and surface composition in $GaZrO_x$ [35], Fig. 2c shows the partial negative TOF-SIMS spectra result in Ga:Zr(1:4), the ions of $GaZrO^-$ (m/z = 176.8), $GaZrO_2^-$(m/z = 192.8), $GaZrO_3^-$(m/z = 208.8), $GaZrO_4^-$(m/z = 224.8), $GaZrO_5^-$(m/z = 240.8) are presented, this result provides strong evidence that the Ga–O–Zr bridges existed in $GaZrO_x$ [20], confirming the introduction of Ga into ZrO_2 formed the solid solution structure with the cation substitution.

To study the morphology and crystallite transformation of metal oxides, TEM and HR-TEM images of sole ZrO_2, Ga:Zr(1:8), Ga:Zr(1:4), Ga:Zr(4:1), and Ga_2O_3 are performed and shown in Fig. 3. As shown in Fig. 3a, sole ZrO_2 shows irregular agglomeration of nanoparticles. After the introduction of Ga and increasing the Ga:Zr atomic ratio, the
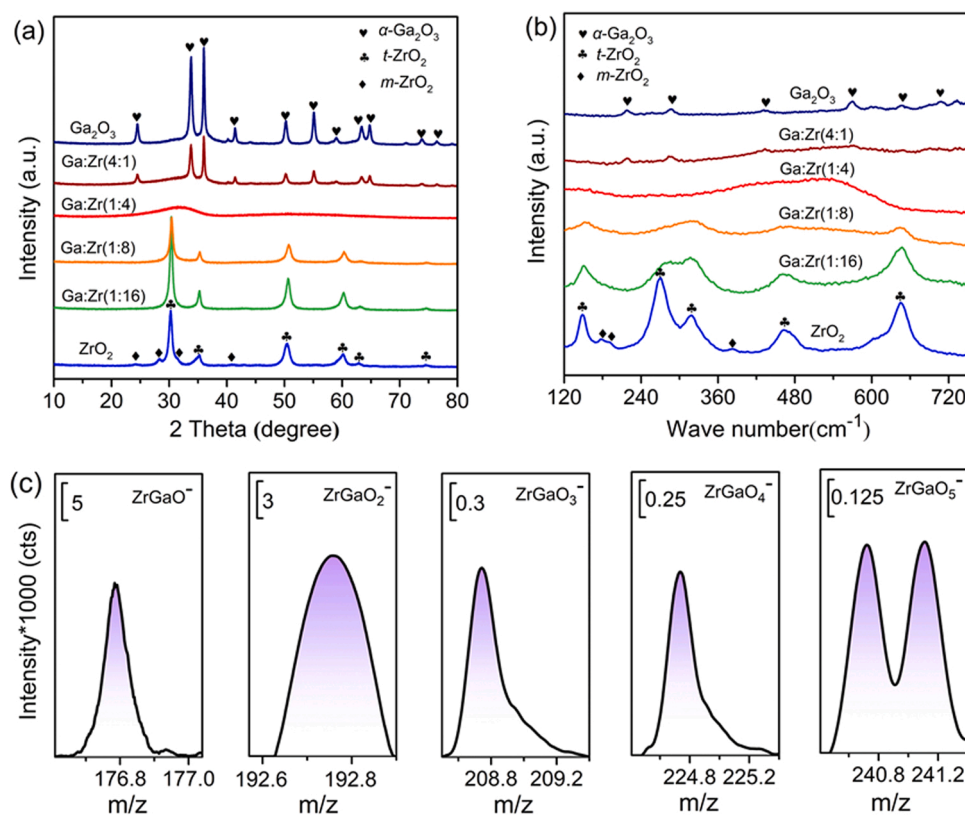
Fig. 2. (a) XRD patterns, (b) Raman spectra of GaZrO$_x$ with various Ga:Zr atomic ratios, and (c) Partial negative TOF-SIMS spectra of the GaZrO$_x$ with Ga:Zr atomic ratio of 1:4.

morphology of GaZrO$_x$ gradually shifts to rod-like morphology, as shown in Fig. 3b-d. In particularly, Ga:Zr(4:1) in Fig. 3d with more content of Ga displays the similar particles morphology to that of sole Ga$_2$O$_3$ (Fig. 3e), which exhibits a regular monodispersed rod-like morphology. The inset HR-TEM image of sole ZrO$_2$ shows a well-defined lattice fringe of 0.299 nm, corresponding to t-ZrO$_2$(011). The introduction of Ga shrank the lattice fringe of Ga:Zr(1:8) to 0.291 nm, suggesting that Ga^{3+} is incorporated into the lattice of ZrO$_2$. Ga:Zr(1:4) exhibits no lattice fringes, which is probably due to the high mutual solubility of Zr and Ga species. Ga:Zr(4:1) shows the lattice fringe of 0.370 nm, which is similar to that of sole Ga$_2$O$_3$ (0.371 nm), corresponding to α-Ga$_2$O$_3$ (012). The HRTEM-EDS images in Fig. 3f demonstrate that the elements of Zr, Ga and O are uniformly dispersed in Ga:Zr (1:4) oxide sample, consistent with XRD and Raman analyses.

3.3. Surface property analysis

XPS spectra results of Ga 2p$_{3/2}$ in metal oxides are shown in Fig. 4a, for sole Ga$_2$O$_3$, the binding energies of Ga 2p$_{3/2}$ at 1118.7 eV is assigned to the bonding of Ga-OH species in Ga(OH)$_3$ [36], which produced from the remnants of growth precursor. The binding energies at 1117.3 eV is attributed to the Ga^{3+} species in Ga$_2$O$_3$ [37], it is found the binding energies for Ga^{3+} species in GaZrO$_x$ is higher than that of Ga$_2$O$_3$, the variation tendency of Ga 2p$_{3/2}$ indicates that the electronic property of the Ga site is modified by the adjacent Zr site, caused by the incorporation of Ga into ZrO$_2$ lattice. The surface oxygen vacancy concentration in GaZrO$_x$ is further studied by O 1s spectra. Three types of O species are observed in O 1 s spectra as shown in Fig. 4b. The peaks centered at the binding energies of 529.5–530.5 eV are attributed to lattice oxygen (O$_L$), the peaks occurred at binding energies of 530.5–531.5 eV is associated with oxygen atoms next to surface oxygen vacancy (O$_V$), and the peaks located at 531.5–532.5 eV are attributed to hydroxyl group (O$_{OH}$) [13, 38,39], the concentrations of these surface oxygen species are listed in

Table S2, as the Ga:Zr atomic ratio increases, the binding energy of O 1s shifts towards higher binding energy, which is due to the formation of Ga–O–Zr structure. Furthermore, it is found that the concentration of O$_V$ firstly increases and then decreases as the Ga:Zr atomic ratio increases, Ga:Zr(1:4) oxide shows the highest O$_V$ concentration of 32.6%, confirming the introduction of an optimal amount of Ga into ZrO$_2$ lattice benefits the formation of large amounts of surface oxygen vacancy. EPR is further used to characterize the O$_V$ concentration in the bulk and surface of metal oxides [40], it is found the EPR signal at g = 2.002, which is presented due to the unpaired electrons trapped on O$_V$, firstly increases and then decreases as the Ga:Zr atomic ratio increases, Ga:Zr (1:4) oxide shows the highest O$_V$ concentration in comparison to the other samples, consistent with the XPS result.

The adsorption ability of CO$_2$ for metal oxides is examined by CO$_2$-TPD. The profiles are shown in Fig. 5. Two distinct desorption regions in the range of 50–150 °C and 280–360 °C are observed and denoted as peak α and β. The low-temperature CO$_2$ desorption peaks centered at ca. 90 °C are attributed to the physical adsorption of CO$_2$ on GaZrO$_x$ oxides surface. While the desorption peaks at high-temperature are ascribed to the strong chemisorption sites [13,14]. The amounts of desorbed CO$_2$ for peak β listed in Table S3 follow the sequence: Ga:Zr(1:4) > Ga:Zr(1:8) > Ga:Zr(1:16) > ZrO$_2$ > Ga:Zr(4:1) > Ga$_2$O$_3$. To evaluate the dissociation ability of H$_2$ of metal oxides, the hydrogenation of ethylene over metal oxides is selected as a probe reaction to represent H$_2$ dissociation ability. The results are shown in Fig. S4. After normalizing the conversion of C$_2$H$_4$, the sole ZrO$_2$ exhibits the lowest H$_2$ dissociation ability (6.9). The H$_2$ dissociation ability enhances after the introduction of Ga into ZrO$_2$ and linearly increases with the increasing of Ga:Zr atomic ratio. In addition, the H$_2$ dissociation ability is not related to the specific surface area as shown in Table S4. Thus, it is concluded that Ga species is mainly responsible for H$_2$ activation. Increasing Ga content leads to an obvious increase of H$_2$ dissociation ability.

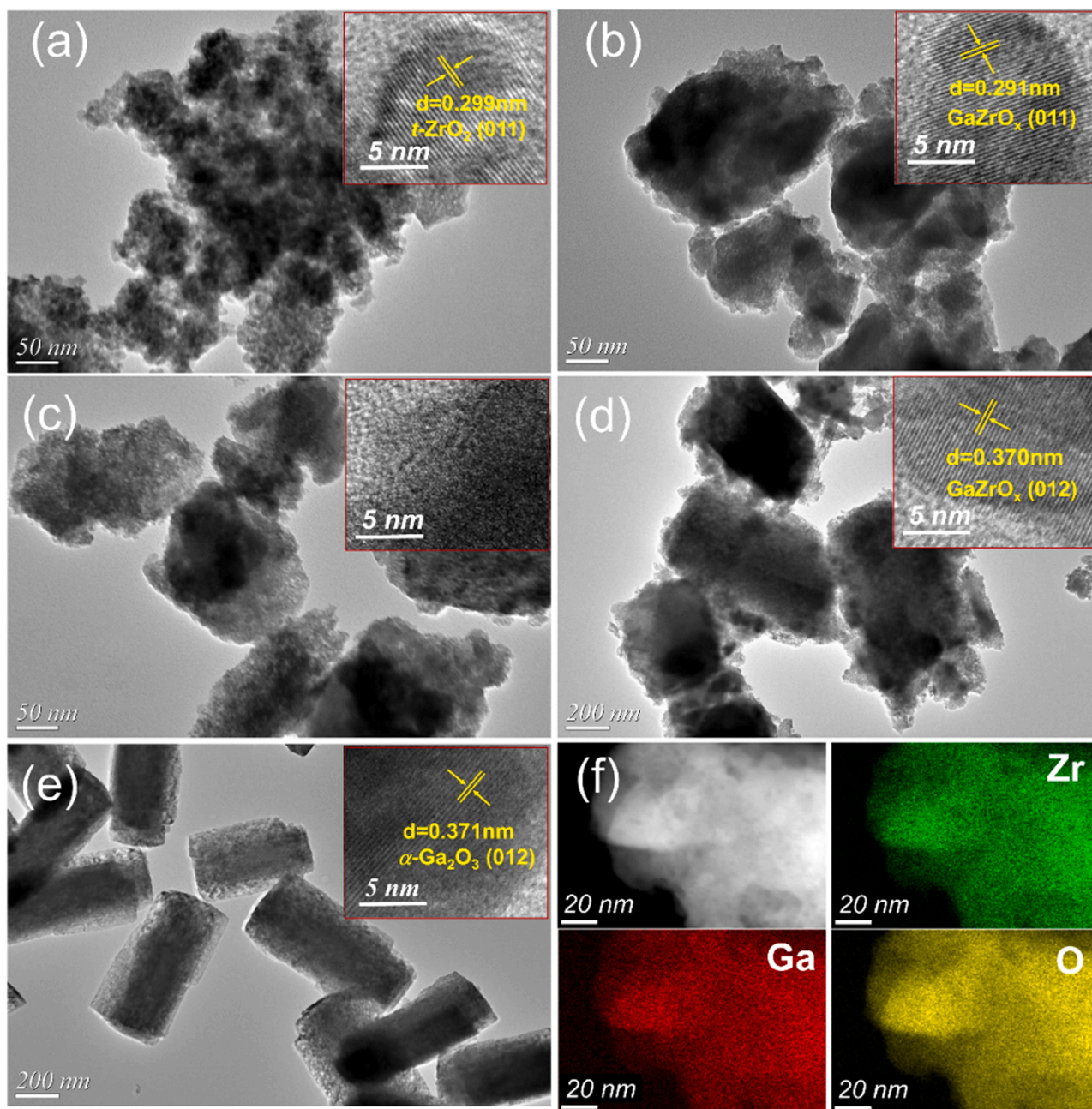Fig. 6 shows the relationship between the catalytic performance and

Fig. 3. TEM images with inset HR-TEM images of metal oxides. (a) ZrO_2, (b) Ga:Zr(1:8), (c) Ga:Zr(1:4), (d) Ga:Zr(4:1), (e) Ga_2O_3, and (f) EDS-mapping diagram of Ga:Zr(1:4).

structure. As shown in Fig. 6a, as the Ga:Zr atomic ratio increases, the surface O_V concentration firstly increases and then decreases, while the H_2 dissociation ability gradually increases. Ga:Zr(1:4) exhibits the highest $C_2^= - C_4^=$ yield among the investigated samples, which possesses the highest surface O_V content with moderate H_2 dissociation ability. As shown in Fig. 6b, it is found that the CO_2 desorption amount shows obvious linear correlation with the surface O_V content, indicating that the presence of surface O_V of $GaZrO_x$ oxides facilitate the adsorption and activation of CO_2. Moreover, the linear correlation between CO_2 conversion and surface O_V content also confirms that the surface O_V serving as the active site promotes the conversion of CO_2, similar finding was also reported to prove that O_V is the active site for CO_2 adsorption and activation over $ZnO-ZrO_2$ oxide, and the formation rate of methanol/ DME intermediate is dominated by the total amount of O_V [41]. As shown in Fig. 6c, it is found that increasing a certain H_2 dissociation

ability (<50) do not obviously influence the O/P ratio, it is inferred that the formation rate of "dissociated H_2" is well matched with the "active CO_2" produced by surface O_V, thus avoiding the second hydrogenation of olefin. While the strong H_2 dissociation ability (>50) makes the "dissociated H_2" is excessive, leading to the more paraffin formation. As shown in Fig. 6d, increasing H_2 dissociation ability in $GaZrO_x$ leads to the total hydrocarbon selectivity firstly increases and then decreases, while the CO selectivity is inverse, which indicates that the moderate H_2 dissociation ability produced by incorporation optimal Ga is more favorable for hydrocarbon products formation. Above analysis suggests that both surface O_V content and H_2 dissociation ability created by synergistic effect of Ga and Zr in $GaZrO_x$ dominates the catalytic performance. The high surface O_V content (32.6%) with moderate H_2 dissociation ability (56.9) over Ga:Zr (1:4) oxide not only improves the CO_2 conversion, but also obviously inhibits the excessive hydrogenation
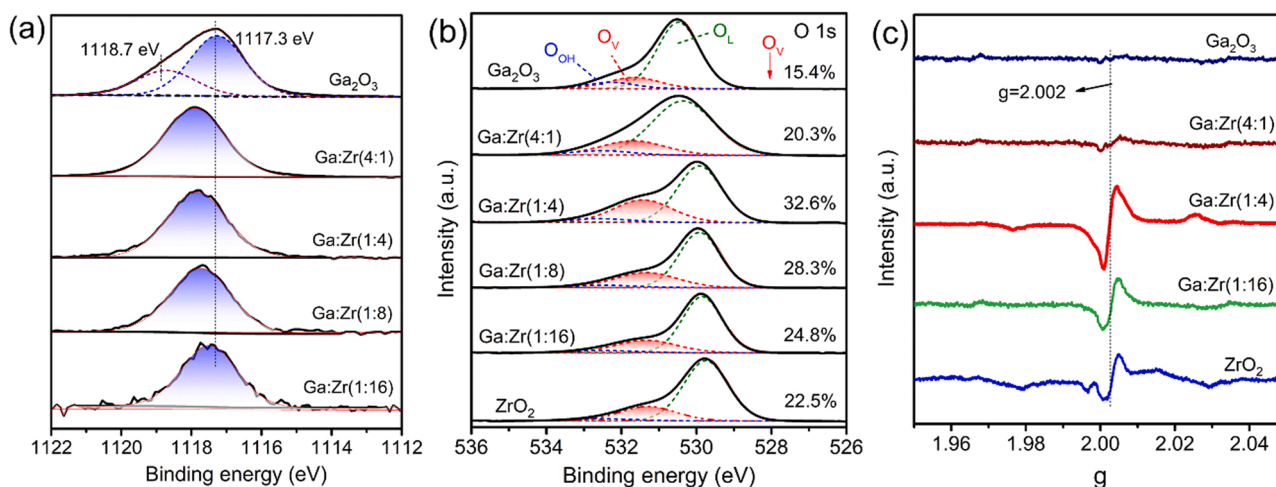
Fig. 4. (a) Ga 2p XPS spectra, (b) O 1 s XPS spectra, and (c) EPR spectra of $GaZrO_x$ with various Ga:Zr atomic ratios.
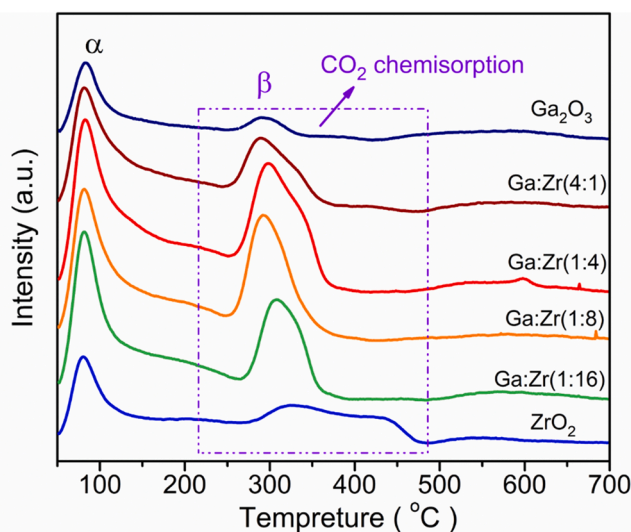

Fig. 5. CO_2-TPD profiles of $GaZrO_x$ with various Ga:Zr atomic ratios.

of $C_2^=$–$C_4^=$ and RWGS reaction, in turn boosting the yield of $C_2^=$–$C_4^=$.

The in-situ DRIFT spectra of metal oxides in H_2 flow under 390 °C are shown in Fig. 7a. The bands at 3745 cm^{-1} and 3668 cm^{-1} are assigned to the terminal hydroxyl and bridged hydroxyl, respectively [42]. All the metal oxides, except the sole Ga_2O_3, exhibit the signals for the terminal hydroxyl and bridged hydroxyl. For the sole Ga_2O_3, only the bridged hydroxyl appears. Interestingly, a new band presents at 1988 cm^{-1}, produced from H_2 dissociation on the surface of Ga_2O_3, is attributed to Ga–H species [29], indicating that the H_2 dissociates on the Ga–O site, producing the O–H and Ga–H group, which is consistent with the previous reports [29,43]. Moreover, the increase of Ga:Zr atomic ratio enhances the intensity of Ga–H band, which is due to the high dissociation ability of Ga species.

To further distinguish the key surface intermediates over Ga:Zr(1:4) oxide, the adsorption of H_2 for CO_2-pretreated Ga:Zr(1:4) oxide at different time is shown in Fig. 7b. After the adsorption of time for 1 min, the peaks ascribed to bidentate formate (bi-HCOO*) at 2968, 2879, 1587, 1386, and 1366 cm^{-1} appear [23,27,44,45]. As the adsorption time increases to 3 min, new apparent peaks at 2933, 2825, 1139 and 1037 cm^{-1} related to methoxide group (CH$_3$O*) are observed and gradually intensified [44,46]. The results indicate that the hydrogenation of CO_2 generates the HCOO*, then HCOO* converts to CH$_3$O*, suggesting that CH$_3$O* is more likely the key intermediate during the

CO_2 hydrogenation process. Subsequently, the Ga:Zr(1:4) oxide was exposed to mixture gas (CO_2 +H_2) at different temperatures, it is found that the peaks ascribed to CH$_3$O* species gradually decrease as the temperature increases, owning to the thermodynamic effect that inhibits the production of CH$_3$O* species at high temperature, but still clearly observed even up to 360 °C and 390 °C, suggesting that Ga:Zr(1:4) oxide can produce and stabilize the CH$_3$O* at high temperature. Upon combination with SAPO-34, as shown in Fig. S5, however, both signal for HCOO* and CH$_3$O* are much weaker, and the new ν(C=C) peaks at $1300 - 1000$ cm^{-1} are observed at high temperature [47], implying that the CH$_3$O* converts to olefin in the presence of SAPO-34.

For comparison, the DRIFT spectra of sole ZrO_2 and Ga_2O_3, treated by CO_2 +H_2 flow at different temperatures are displayed in Fig. 7c and Fig. 7d, and other $GaZrO_x$ with Ga:Zr atomic ratio of 1:16, 1:8, and 4:1 are shown in Fig. S6. The sole ZrO_2 shows that only exhibits the strong signal for HCOO* (2965, 2878, 1585, 1385, 1366) at 240–420 °C, and no signal for CH$_3$O* is observed (Fig. 7c), the results indicate that the formation of HCOO* species via CO_2 hydrogenation is a facile step, which is not influenced by weak H_2 dissociation ability of ZrO_2. While the hydrogenation of HCOO* to form CH$_3$O* is dominated by H_2 dissociation of metal oxide. It is found the introduction of Ga can obviously boost the conversion of HCOO* to CH$_3$O* (Fig. S6), which is due to the introduction of Ga accelerate the H_2 dissociation, confirming the vital role of Ga species in the conversion HCOO* to form CH$_3$O*; however, the $GaZrO_x$ with excessive Ga leads to the obvious decrease the intensity of HCOO* at high temperature (Fig. S6c). For sole Ga_2O_3 as shown in Fig. 7d, the signals for both HCOO* (2973, 2889, 1599, 1385, 1368 cm^{-1}) and CH$_3$O* (2938, 2832 cm^{-1}) are detected between the temperature of 270 °C and 360 °C. However, the intensity of these peaks are extremely weak, especially at high temperature (>360 °C), implying that the formation of the HCOO* and CH$_3$O* over sole Ga_2O_3 or $GaZrO_x$ at high Ga content are obviously limited at high temperature.

Interestingly, it is found that the peak positions of HCOO*species for all the $GaZrO_x$ oxides are well accordance with the ZrO_2, and the peak positions of both HCOO* and CH$_3$O* in $GaZrO_x$ oxides are much lower than Ga_2O_3 (Fig. 7, Fig. S6), it is reasonable to deduce that the oxygen vacancy at Zr site in $GaZrO_x$ is mainly responsible for CO_2 adsorption, activation, while Ga sites provide the essential hydrogenation sites, the moderate H_2 dissociation ability produced by incorporation optimal Ga boosts CO_2 hydrogenation to CH$_3$O* intermediate at high temperature.

3.4. DFT calculations

To illustrate above experimental results and gain a deeper insight of the CO_2/H_2 adsorption, activation, and the hydrogenation mechanism
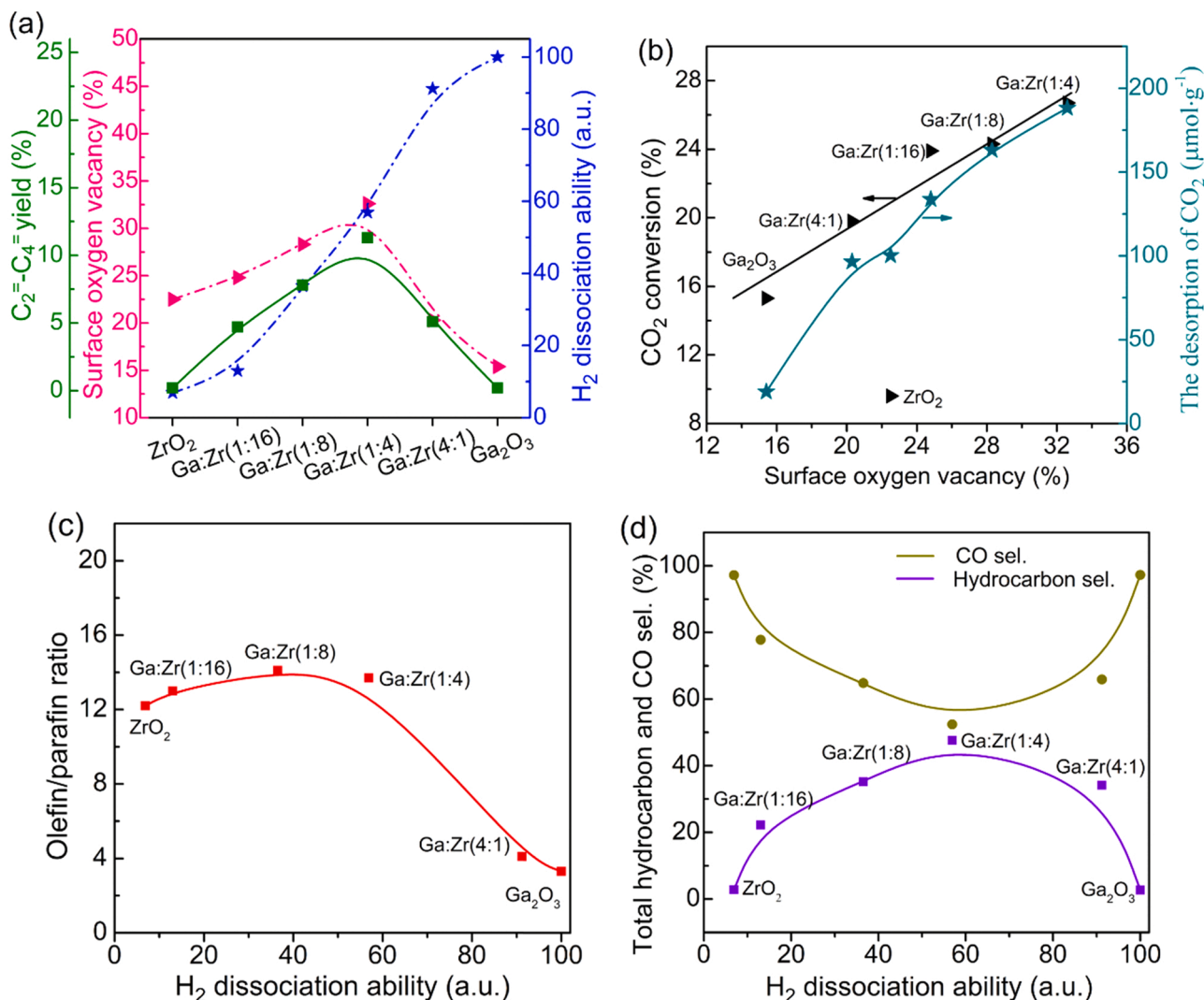
Fig. 6. Relationship between catalyst activity, CO_2 desorption amount, and surface oxygen vacancy content, H_2 dissociation ability. Reaction condition: 390 ℃, 3.0 MPa, GHSV= 3000 mL·h^{-1}·g^{-1}.

over GaZrO$_x$ oxide, DFT calculations are performed by considering the O$_V$-ZrO$_2$(101), O$_V$-GaZrO$_x$(101) and O$_V$-Ga$_2$O$_3$(012) surface model (Fig S7).

The activation of CO_2/H_2 over O$_V$-GaZrO$_x$(101) is shown in Fig. 8. the CO_2 chemisorption at the O$_V$ results in the formation of C–Zr and O–Zr bond with the adsorption energy of -26.2 kJ·mol^{-1}, the C–O bond lengths (C–O$_1$ and C–O$_2$) of 1.213 and 1.266 Å and the bent O–C–O angle of 138.180° (Fig. 8a), notably, compared to the perfect GaZrO$_x$(101), DFT result suggests the presence of oxygen vacancy promotes CO_2 adsorption and activation, which is consistent with the experimental and characterized results (Fig. S8). The electronic property of adsorbed CO_2 on O$_V$-GaZrO$_x$(101) is examined by differential charge density and Bader charge analysis, it is found that the oxidation state of C atom in CO_2 decreased, the C atom of CO_2 loses 1.44 |e|, both O$_1$ and O$_2$ atoms of CO_2 carry extra 1.12 and 0.97 |e|, in which the electron depletion region appears around the C atom, and the asymmetric electron enrichment area are around the adjacent O atoms. Confirming that CO_2 activation is attributed to the electrons trapped in the O$_V$ site.

For the adsorption of H_2, as shown in Fig. 8b, H_2 can spontaneously dissociate into two H atoms, which are adsorbed at the Ga and O sites on the O$_V$-GaZrO$_x$(101), two H atoms are elongated to 2.773 Å. For comparison, H_2 is typically physisorbed at the top-Zr site on O$_V$-ZrO$_2$(101) with the H–H bond length of 0.755 Å (Fig. S9a), while H_2 can also

spontaneously dissociate into two H atoms, which are adsorbed at two Ga sites on O$_V$-Ga$_2$O$_3$(012), two H atoms are elongated to 3.085 Å (Fig. S9b). Which indicated that ZrO$_2$ has weak H_2 dissociation ability, the introduction of Ga to ZrO$_2$ obviously enhances H_2 dissociation ability, which well confirms our experimental and characterized results. The differential charge density and Bader charge analysis are carried out for two adsorbed H atoms from H_2 dissociative adsorption on O$_V$-GaZrO$_x$(101). H adsorbed at the O site loses 0.68 |e| and become positively charged, while H adsorbed at the Ga site carry extra 0.34 |e| and become negatively charged. Thus, the Ga–O bridge site can act as the active center to produce an H$^{\delta-}$ located at the Ga site and an H$^{\delta+}$ located at the O site, which is attributed to the local charge polarization along the Ga–O bond.

Two major reaction pathways of CO_2 hydrogenation, the formate and RWGS pathways, are considered over O$_V$-GaZrO$_x$(101) model, as shown in Fig. 9a. The corresponding structures involving in CO_2 hydrogenation through formate pathway are presented in Fig. 9b. The calculated activation barrier (G$_a$) and reaction energy (ΔG) are listed in Table S6. In the formate pathway, the adsorbed CO_2 reacts with the nearby Ga–H$^{\delta-}$ to form HCOO* , which has the activation free energy of 13.6 kJ·mol^{-1}, and it is strongly exothermic by -124.4 kJ·mol^{-1}. Suggesting that the reaction of adsorbed CO_2 with dissociated H* to form HCOO* species is energetically very favorable, which is consistent with the in-situ DRIFT
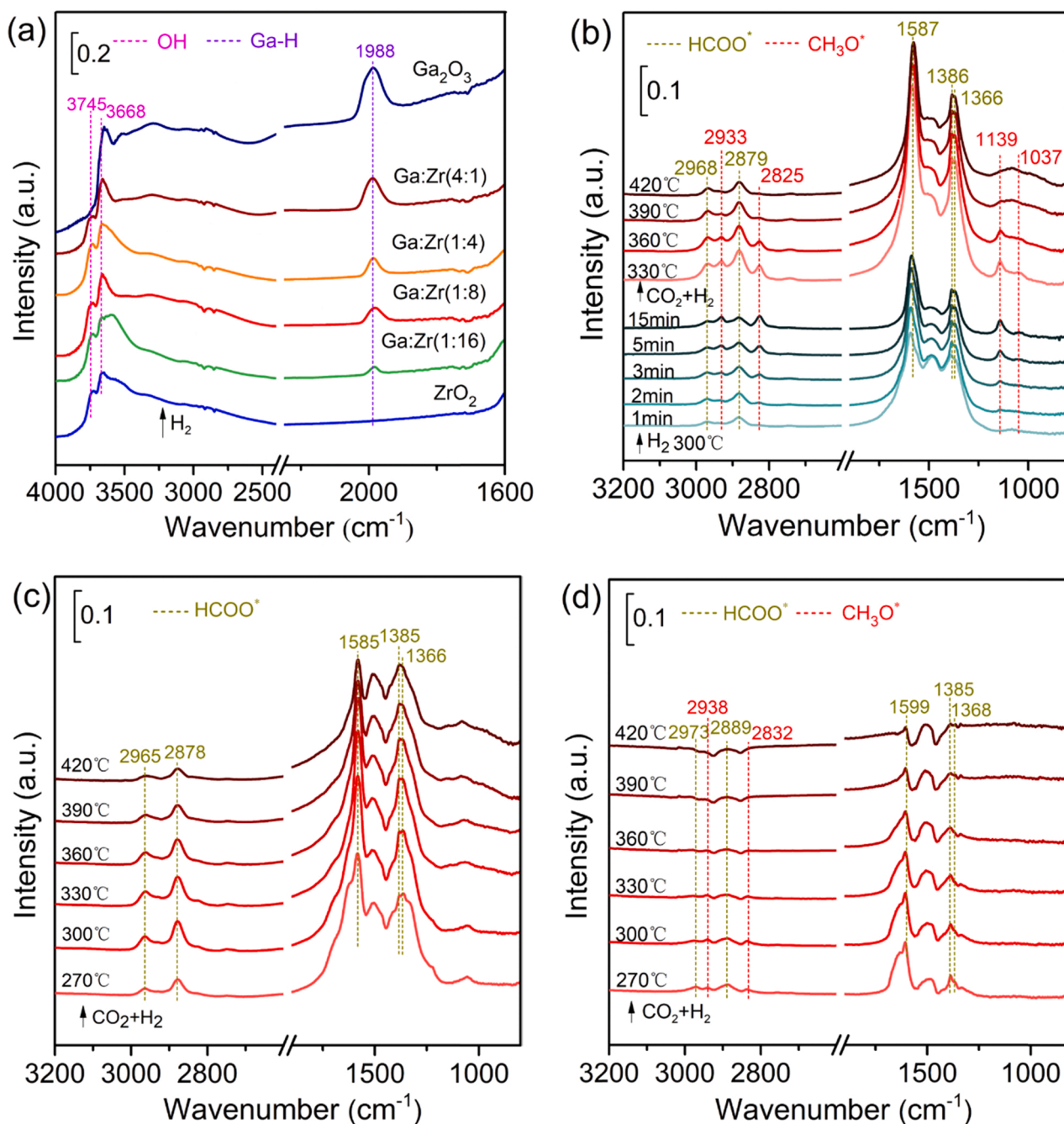
Fig. 7. In-situ DRIFT spectra. (a) GaZrO$_x$ with various Ga:Zr atomic ratios treated by H$_2$ flow at 390 °C, (b) CO$_2$-pretreated Ga:Zr(1:4) oxide treated by H$_2$ flow at 300 °C and subsequent switched to CO$_2$ +H$_2$ at different temperatures, (c) sole ZrO$_2$ and (d) sole Ga$_2$O$_3$ treated by CO$_2$ +H$_2$ flow at different temperatures.

results. HCOO* hydrogenation to H$_2$COO* has the activation free energy of 49.2 kJ·mol^{-1}, and it is endothermic by 37.2 kJ·mol^{-1}. Then, H$_2$COO* hydrogenation to H$_2$COOH* has a small activation free energy of 10.6 kJ·mol^{-1} with the reaction energy of −44.9 kJ·mol^{-1}. Subsequently, the C–O bond cleavage of H$_2$COOH* can produce CH$_2$O* and OH* adsorbed at the bridge Zr–Zr and Ga sites, respectively, which is identified as the rate-determining step of the overall reaction, correspondingly, this reaction has a higher activation free energy of 86.7 kJ·mol^{-1}, and it is exothermic by 55.9 kJ·mol^{-1}. Further, CH$_2$O* hydrogenation to CH$_3$O* is energetically favorable with the activation and reaction free energies of 21.6 and −72.1 kJ·mol^{-1}, respectively. Finally, CH$_3$OH formed by the hydrogenation of CH$_3$O* - with activation and reaction free energies of 79.3 and 79.2 kJ·mol^{-1}. Notably, it is found that CH$_3$OH cannot be stably adsorbed on the surface

Ov-GaZrO$_x$(101) due to its much easier dissociation into CH$_3$O* and H* species in kinetics (Fig. S10). It is concluded that CH$_3$O* is more likely the reaction intermediate linked the metal oxide and SAPO-34.

In the RWGS pathway, CO$_2$ hydrogenation to form *trans*-COOH* has the activation and reaction free energies of 110.8 and 7.9 kJ·mol^{-1}, respectively, which is kinetically and thermodynamically unfavorable compared to HCOO* formation, meanwhile, *trans*-COOH* formation is the rate-determining step of the overall reaction. Then, *trans*-COOH* is isomerized into *cis*-COOH* with the activation and reaction free energies of 27.7 and 26.6 kJ·mol^{-1}, respectively. CO* can be produced by the dissociation of *cis*-COOH* with the activation and reaction free energies of 28.1 and −43.0 kJ·mol^{-1}, respectively. The weakly bonded CO* prefers to desorb from the metal oxide surface instead of further hydrogenation, making the CO as the main product. Hence, it can be
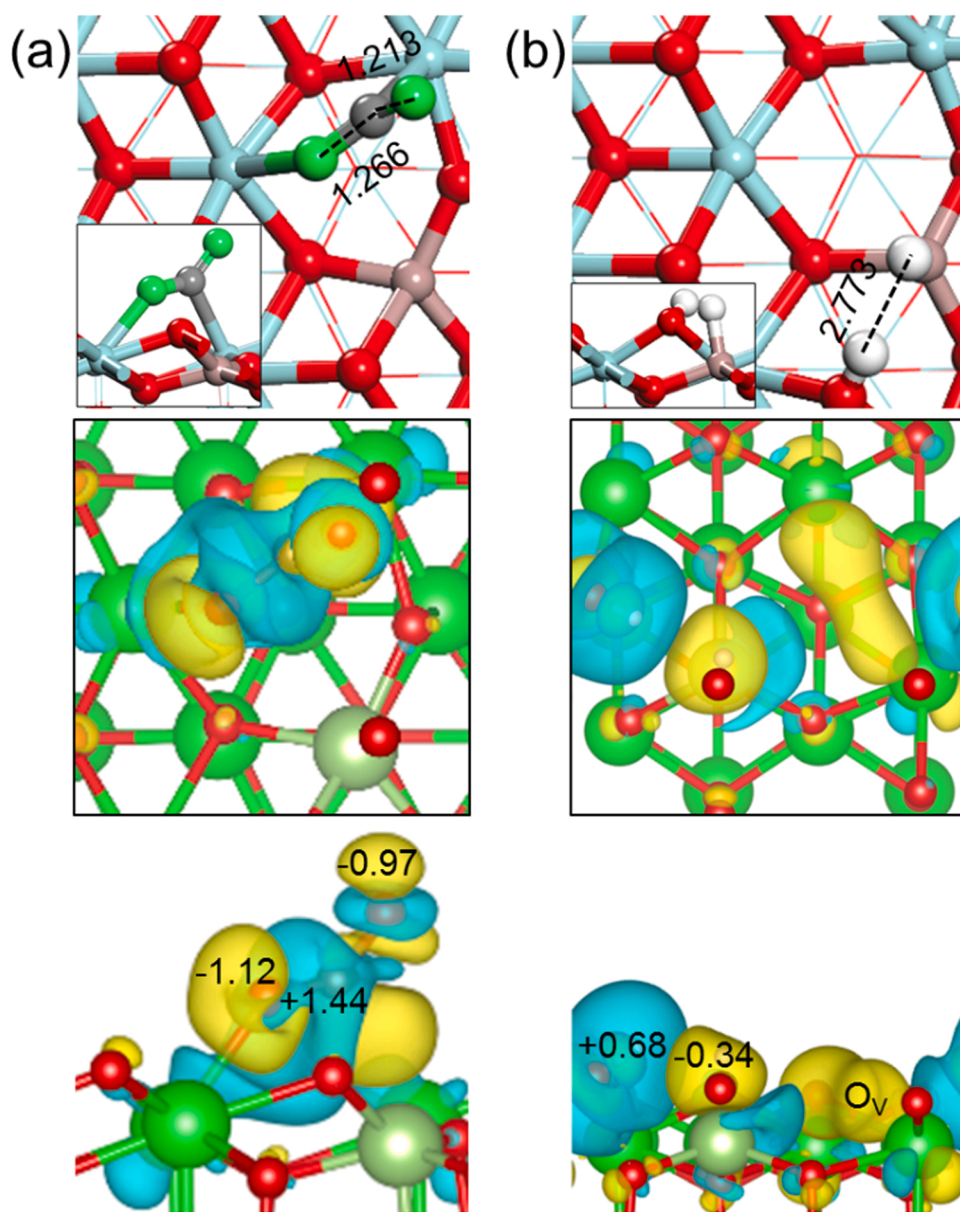
Fig. 8. The stable adsorption configurations and differential charge density plots and Bader charge of CO_2 (a) and H_2 species (b) adsorbed on O_V-$GaZrO_x$(101) surface. Blue, brown and white balls represent Zr, Ga and H atoms, respectively. Red and green balls correspond to O atom of catalyst surface and CO_2 species, respectively; Cyan and yellow contours represent electron depression and accumulation, respectively. (For interpretation of the references to colour in this figure, the reader is referred to the web version of this article.)

concluded that the formate pathway, dominantly contributes to the formation of CH_3O^* intermediate rather than RWGS pathway.

Based on the above discussion, the catalytic mechanism of CO_2 hydrogenation over $GaZrO_x$/SAPO-34 catalyst is shown in Fig. 10. Firstly, the CO_2 absorbs on the surface O_V near Zr-Zr sites to be activated, and simultaneously, the H_2 absorbs on adjacent Ga sites to be dissociated, forming Ga–$H^{\delta-}$ and O–$H^{\delta+}$. Activated CO_2 * could either react with Ga–$H^{\delta-}$ to form HCOO* and CH_3O^* via successtive hydrogenation, or combine with O–$H^{\delta+}$ to form COOH* , followed by dissociation to form CO (RWGS reaction). The formate pathway for CH_3O^* formation is competed with RWGS reaction, which is mainly determined by the H_2 dissociation ability of $GaZrO_x$ oxide. The weak H_2 dissociation ability over $GaZrO_x$ impedes the hydrogenation of HCOO* , while the strong H_2 dissociation ability suppresses HCOO* formation at high temperature. Only the moderate H_2 dissociation ability produced by introduction of optimized Ga to ZrO_2 benefits CO_2 hydrogenation to form and stabilize HCOO* , and further hydrogenation to CH_3O^* intermediate at high temperature, the generated CH_3O^* at high temperature would supply a well temperature compatibility for its further conversion over SAPO-34, which favors the $C_2^=$–$C_4^=$ yield.

4. Conclusions

A highly active and selective $GaZrO_x$/SAPO-34 bifunctional catalyst for CO_2 hydrogenation into $C_2^=$–$C_4^=$ was successfully prepared. Under a condition of 390 ℃, 3.0 MPa and 3000 mL·h^{-1}·g^{-1}, the selectivity for $C_2^=$–$C_4^=$ reached 88.8% in hydrocarbons at a high CO_2 conversion of 26.7%, and the light olefin yield is as high as 11.3%. As the Ga:Zr atomic ratio increases, the surface oxygen vacancy content firstly increases from 22.5% to 32.6% and then decreases to 15.4%, while the H_2 dissociation ability gradually increases. CO_2 adsorption ability has a linear relationship with the oxygen vacancy content of the $GaZrO_x$, indicating that the oxygen vacancy is the catalytic site of adsorption and activation of CO_2. The H_2 dissociation ability of $GaZrO_x$ plays the crucial role for CH_3O^* intermediate formation and olefin/paraffin ratio, it is found that the weak H_2 dissociation ability over $GaZrO_x$ impedes the hydrogenation of HCOO* , while the strong H_2 dissociation ability suppresses HCOO* formation at high temperature. The moderate H_2 dissociation ability produced by incorporation optimal Ga benefits CO_2 hydrogenation to HCOO* , and further to CH_3O^* intermediate via successive hydrogenation at high temperature, while obviously inhibits RWGS
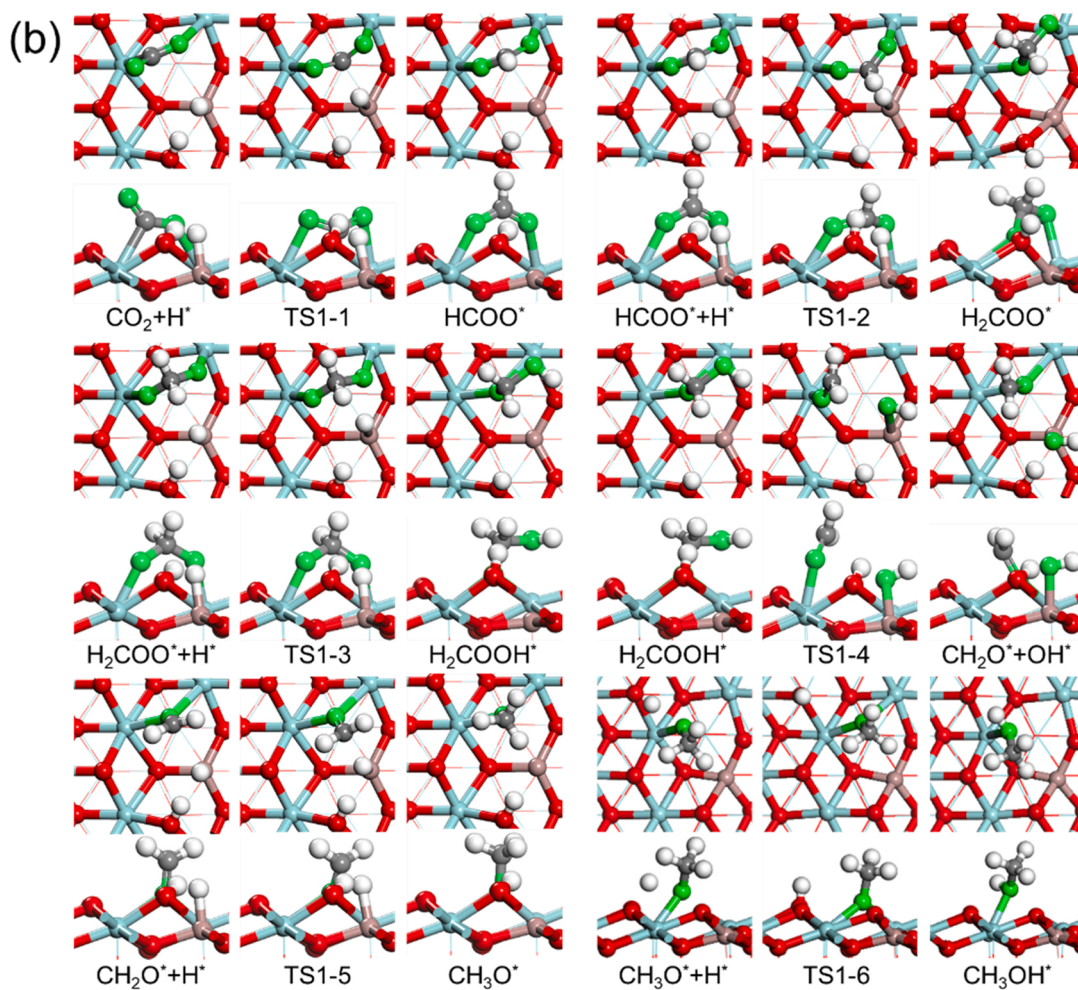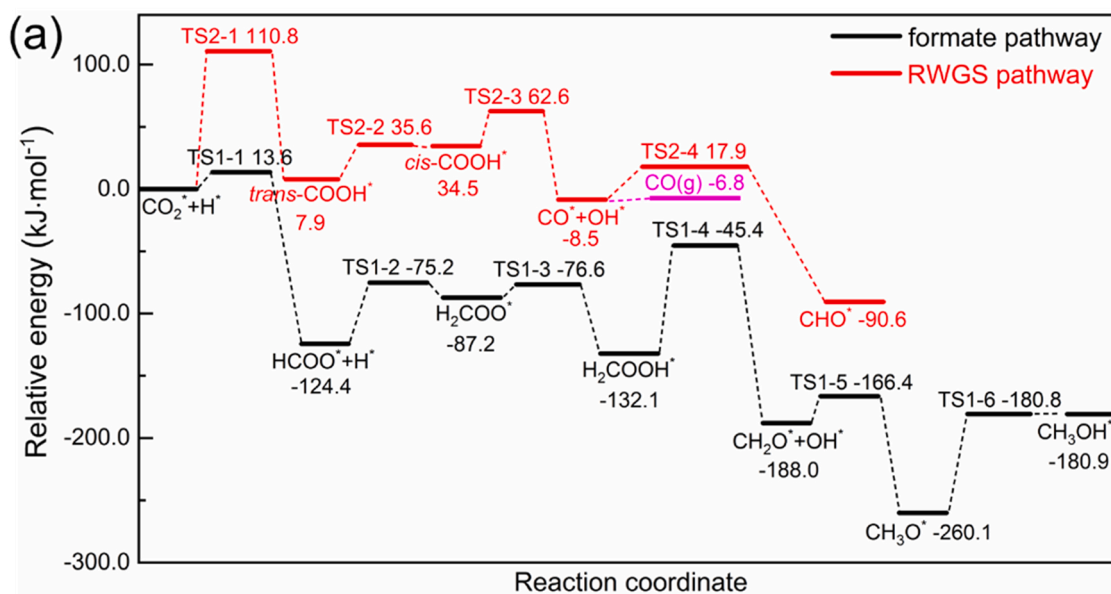
Fig. 9. (a) The potential energy profiles of CO_2 hydrogenation to form CH_3OH and CO on O_V-$GaZrO_x$(101) surface. (b) The structures of initial states, transition states and final states through the formate pathway.
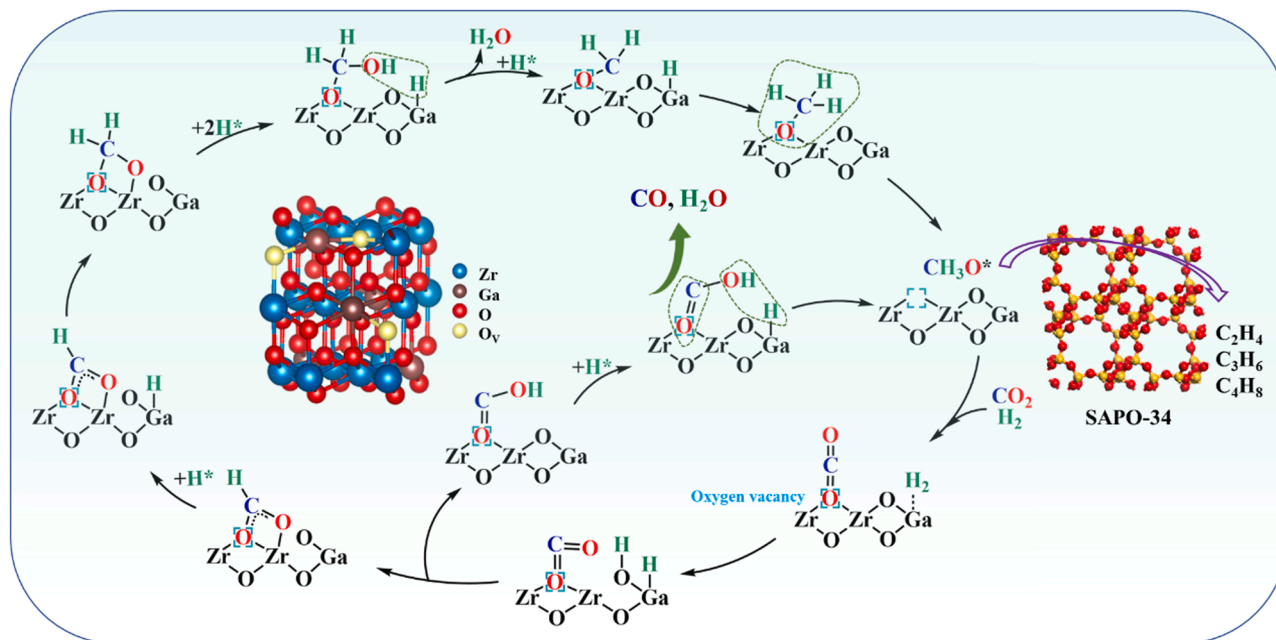
Fig. 10. The mechanism for CO_2 hydrogenation over $GaZrO_x$/SAPO-34 catalyst.

reaction and excessive hydrogenation of $C_2^=$–$C_4^=$, in turn boosting yield of $C_2^=$–$C_4^=$. Mechanistic study shows that formate pathway, dominantly contributes to the formation of CH_3O^* intermediate rather than RWGS pathway. This work provides a possibility to develop highly active and selective $GaZrO_x$ combined with other zeolites such as SSZ-39, H-ZSM-5 for synthesis high value-added chemicals (e.g., LPG, liquid fuels, aromatics) from CO_2 conversion.

CRediT authorship contribution statement

Peng Zhang: Methodology, Experiment, Data curation, Writing – original draft. **Lixuan Ma:** Simulation, Writing – original draft for simulation section. **Fanhui Meng**: Conceptualization, Investigation, Analysis, Writing – review & editing, Funding acquisition. **Lina Wang:** Investigation, Data curation. **Riguang Zhang:** Simulation, Software, Writing – review & editing, Supervision. **Guinan Yang:** Investigation, Data curation. **Zhong Li**: Conceptualization, Supervision, Funding acquisition. All authors analyzed the data and discussed the results.

Declaration of Competing Interest

The authors declare that they have no known competing financial interests or personal relationships that could have appeared to influence the work reported in this paper.

Acknowledgments

Appendix A. Supporting information

Supplementary data associated with this article can be found in the online version at doi:10.1016/j.apcatb.2021.121042.

References

[1] W. Zhou, K. Cheng, J. Kang, C. Zhou, V. Subramanian, Q. Zhang, Y. Wang, New horizon in C1 chemistry: breaking the selectivity limitation in transformation of syngas and hydrogenation of CO_2 into hydrocarbon chemicals and fuels, Chem. Soc. Rev. 48 (2019) 3193–3228.
[2] H. Ge, B. Zhang, H. Liang, M. Zhang, K. Fang, Y. Chen, Y. Qin, Photocatalytic conversion of CO_2 into light olefins over TiO_2 nanotube confined Cu clusters with high ratio of Cu^+, Appl. Catal. B-Environ. 263 (2020), 118133.
[3] Z. Zhao, J. Jiang, F. Wang, An economic analysis of twenty light olefin production pathways, J. Energy Chem. 56 (2021) 193–202.
[4] C.G. Visconti, M. Martinelli, L. Falbo, A. Infantes-Molina, L. Lietti, P. Forzatti, G. Iaquaniello, E. Palo, B. Picutti, F. Brignoli, CO_2 hydrogenation to lower olefins on a high surface area K-promoted bulk Fe-catalyst, Appl. Catal. B-Environ. 200 (2017) 530–542.
[5] P. Zhang, F. Han, J. Yan, X. Qiao, Q. Guan, W. Li, N-doped ordered mesoporous carbon (N-OMC) confined Fe_3O_4-FeC_x heterojunction for efficient conversion of CO_2 to light olefins, Appl. Catal. B-Environ. 299 (2021) 120639.
[6] H.M. Torres Galvis, K.P. de Jong, Catalysts for production of lower olefins from synthesis gas: A review, ACS Catal. 3 (2013) 2130–2149.
[7] Z. Ma, M.D. Porosoff, Development of tandem catalysts for CO_2 hydrogenation to olefins, ACS Catal. 9 (2019) 2639–2656.
[8] S. Wang, L. Zhang, W. Zhang, P. Wang, Z. Qin, W. Yan, M. Dong, J. Li, J. Wang, L. He, U. Olsbye, W. Fan, Selective conversion of CO_2 into propene and butene, Chem 6 (2020) 3344–3363.
[9] J. Wei, R. Yao, Y. Han, Q. Ge, J. Sun, Towards the development of the emerging process of CO_2 heterogenous hydrogenation into high-value unsaturated heavy hydrocarbons, Chem. Soc. Rev. 50 (2021) 10764–10805.
[10] Q.M. Sun, Z.K. Xie, J.H. Yu, The state-of-the-art synthetic strategies for SAPO-34 zeolite catalysts in methanol-to-olefin conversion, Natl. Sci. Rev. 5 (2018) 542–558.
[11] Z. Li, J. Wang, Y. Qu, H. Liu, C. Tang, S. Miao, Z. Feng, H. An, C. Li, Highly selective conversion of carbon dioxide to lower olefins, ACS Catal. 7 (2017) 8544–8548.
[12] J. Gao, C. Jia, B. Liu, Direct and selective hydrogenation of CO_2 to ethylene and propene by bifunctional catalysts, Catal. Sci. Technol. 7 (2017) 5602–5607.
[13] P. Gao, S. Dang, S. Li, X. Bu, Z. Liu, M. Qiu, C. Yang, H. Wang, L. Zhong, Y. Han, Q. Liu, W. Wei, Y. Sun, Direct production of lower olefins from CO_2 conversion via bifunctional catalysis, ACS Catal. 8 (2018) 571–578.
[14] S. Dang, P. Gao, Z. Liu, X. Chen, C. Yang, H. Wang, L. Zhong, S. Li, Y. Sun, Role of zirconium in direct CO_2 hydrogenation to lower olefins on oxide/zeolite bifunctional catalysts, J. Catal. 364 (2018) 382–393.
[15] X. Liu, M. Wang, C. Zhou, W. Zhou, K. Cheng, J. Kang, Q. Zhang, W. Deng, Y. Wang, Selective transformation of carbon dioxide into lower olefins with a bifunctional catalyst composed of $ZnGa_2O_4$ and SAPO-34, Chem. Commun. 54 (2018) 140–143.
[16] X. Liu, M. Wang, H. Yin, J. Hu, K. Cheng, J. Kang, Q. Zhang, Y. Wang, Tandem catalysis for hydrogenation of CO and CO_2 to lower olefins with bifunctional catalysts composed of spinel oxide and SAPO-34, ACS Catal. 10 (2020) 8303–8314.
[17] O. Martin, A.J. Martín, C. Mondelli, S. Mitchell, T.F. Segawa, R. Hauert, C. Drouilly, D. Curulla-Ferré, J. Pérez-Ramírez, Indium oxide as a superior catalyst

for methanol synthesis by CO_2 hydrogenation, Angew. Chem. -Int. Ed. 55 (2016) 6261–6265.

[18] N. Akkharaphatthawon, N. Chanlek, C.K. Cheng, M. Chareonpanich, J. Limtrakul, T. Witoon, Tuning adsorption properties of $Ga_xIn_{2-x}O_3$ catalysts for enhancement of methanol synthesis activity from CO_2 hydrogenation at high reaction temperature, Appl. Surf. Sci. 489 (2019) 278–286.

[19] J. Wang, C. Tang, G. Li, Z. Han, Z. Li, H. Liu, F. Cheng, C. Li, High-performance $MaZrO_x$ (Ma = Cd, Ga) solid-solution catalysts for CO_2 hydrogenation to methanol, ACS Catal. 9 (2019) 10253–10259.

[20] W.-H. Feng, M.-M. Yu, L.-J. Wang, Y.-T. Miao, M. Shakouri, J. Ran, Y. Hu, Z. Li, R. Huang, Y.-L. Lu, D. Gao, J.-F. Wu, Insights into bimetallic oxide synergy during carbon dioxide hydrogenation to methanol and dimethyl ether over $GaZrO_x$ oxide catalysts, ACS Catal. 11 (2021) 4704–4711.

[21] K. Li, J.G. Chen, CO_2 hydrogenation to methanol over ZrO_2-containing catalysts: Insights into ZrO_2 induced synergy, ACS Catal. 9 (2019) 7840–7861.

[22] J. Liu, Y. He, L. Yan, K. Li, C. Zhang, H. Xiang, X. Wen, Y. Li, Nano-sized ZrO_2 derived from metal–organic frameworks and their catalytic performance for aromatic synthesis from syngas, Catal. Sci. Technol. 9 (2019) 2982–2992.

[23] E.M. Kock, M. Kogler, T. Bielz, B. Klotzer, S. Penner, In situ FT-IR spectroscopic study of CO_2 and CO adsorption on Y_2O_3, ZrO_2, and yttria-stabilized ZrO_2, J. Phys. Chem. C. 117 (2013) 17666–17673.

[24] M.S. Frei, C. Mondelli, A. Cesarini, F. Krumeich, R. Hauert, J.A. Stewart, D. Curulla Ferré, J. Pérez-Ramírez, Role of zirconia in indium oxide-catalyzed CO_2 hydrogenation to methanol, ACS Catal. 10 (2020) 1133–1145.

[25] Y. Wang, G. Wang, L.I. van der Wal, K. Cheng, Q. Zhang, K.P. de Jong, Y. Wang, Visualizing element migration over bifunctional metal-zeolite catalysts and its impact on catalysis, Angew. Chem. -Int. Ed. 60 (2021) 17735–17743.

[26] K. Cheng, B. Gu, X.L. Liu, J.C. Kang, Q.H. Zhang, Y. Wang, Direct and highly selective conversion of synthesis gas into lower olefins: Design of a bifunctional catalyst combining methanol synthesis and carbon-carbon coupling, Angew. Chem. -Int. Ed. 55 (2016) 4725–4728.

[27] J. Wang, G. Li, Z. Li, C. Tang, Z. Feng, H. An, H. Liu, T. Liu, C. Li, A highly selective and stable ZnO-ZrO_2 solid solution catalyst for CO_2 hydrogenation to methanol, Sci. Adv. 3 (2017), e1701290.

[28] W. Jochum, S. Penner, K. Föttinger, R. Kramer, G. Rupprechter, B. Klötzer, Hydrogen on polycrystalline β-Ga_2O_3: Surface chemisorption, defect formation, and reactivity, J. Catal. 256 (2008) 268–277.

[29] Y.-x Pan, D. Mei, C.-j Liu, Q. Ge, Hydrogen adsorption on Ga_2O_3 Surface: A combined experimental and computational study, J. Phys. Chem. C. 115 (2011) 10140–10146.

[30] P. Zhang, F. Meng, X. Li, L. Yang, P. Ma, Z. Li, Excellent selectivity for direct conversion of syngas to light olefins over a Mn–Ga oxide and SAPO-34 bifunctional catalyst, Catal. Sci. Technol. 9 (2019) 5577–5581.

[31] G. Kresse, J. Furthmüller, Efficient iterative schemes for ab initio total-energy calculations using a plane-wave basis set, Phys. Rev. B 54 (1996) 11169–11186.

[32] G. Kresse, J. Hafner, Ab initio molecular dynamics for open-shell transition metals, Phys. Rev. B 48 (1993) 13115–13118.

[33] M. Mokhtar, S.N. Basahel, T.T. Ali, Effect of synthesis methods for mesoporous zirconia on its structural and textural properties, J. Mater. Sci. 48 (2013) 2705–2713.

[34] S. Ni, Q. Chen, J. Liu, S. Yang, T. Li, X. Yang, J. Zhao, New insights into the Li-storage mechanism in α-Ga_2O_3 anode and the optimized electrode design, J. Power Sources 433 (2019), 126681.

[35] Y. Li, W. Han, R. Wang, L.-T. Weng, A. Serrano-Lotina, M.A. Bañares, Q. Wang, K. L. Yeung, Performance of an aliovalent-substituted $CoCeO_x$ catalyst from bimetallic MOF for VOC oxidation in air, Appl. Catal. B-Environ. 275 (2020), 119121.

[36] W. Jevasuwan, T. Maeda, N. Miyata, M. Oda, T. Irisawa, T. Tezuka, T. Yasuda, Self-limiting growth of ultrathin Ga_2O_3 for the passivation of Al_2O_3/InGaAs interfaces, Appl. Phys. Express 7 (2013), 011201.

[37] J. Tao, H.-L. Lu, Y. Gu, H.-P. Ma, X. Li, J.-X. Chen, W.-J. Liu, H. Zhang, J.-J. Feng, Investigation of growth characteristics, compositions, and properties of atomic layer deposited amorphous Zn-doped Ga_2O_3 films, Appl. Surf. Sci. 476 (2019) 733–740.

[38] H. He, X.T. Lin, S.J. Li, Z. Wu, J.H. Gao, J.L. Wu, W. Wen, D.Q. Ye, M.L. Fu, The key surface species and oxygen vacancies in $MnO_x(0.4)$-CeO_2 toward repeated soot oxidation, Appl. Catal. B-Environ. 223 (2018) 134–142.

[39] S. Wang, P. Wang, D. Shi, S. He, L. Zhang, W. Yan, Z. Qin, J. Li, M. Dong, J. Wang, U. Olsbye, W. Fan, Direct conversion of syngas into light olefins with low CO_2 emission, ACS Catal. 10 (2020) 2046–2059.

[40] H. Chen, Y. Xu, K. Zhu, H. Zhang, Understanding oxygen-deficient La_2CuO_4-δperovskite activated peroxymonosulfate for bisphenol A degradation: The role of localized electron within oxygen vacancy, Appl. Catal. B-Environ. 284 (2021), 119732.

[41] C. Zhou, J. Shi, W. Zhou, K. Cheng, Q. Zhang, J. Kang, Y. Wang, Highly active ZnO-ZrO_2 aerogels integrated with H-ZSM-5 for aromatics synthesis from carbon dioxide, ACS Catal. 10 (2020) 302–310.

[42] T. Merle-Méjean, P. Barberis, S.B. Othmane, F. Nardou, P.E. Quintard, Chemical forms of hydroxyls on/in Zirconia: An FT-IR study, J. Eur. Ceram. Soc. 18 (1998) 1579–1586.

[43] S.E. Collins, M.A. Baltanás, A.L. Bonivardi, Hydrogen chemisorption on gallium oxide polymorphs, Langmuir 21 (2005) 962–970.

[44] J. Kondo, H. Abe, Y. Sakata, K.-i Maruya, K. Domen, T. Onishi, Infrared studies of adsorbed species of H_2, CO and CO_2 over ZrO_2, J. Chem. Soc., Faraday Trans. 1 (84) (1988) 511–519.

[45] F. Meng, X. Li, P. Zhang, L. Yang, G. Yang, P. Ma, Z. Li, Highly active ternary oxide $ZrCeZnO_x$ combined with SAPO-34 zeolite for direct conversion of syngas into light olefins, Catal. Today 368 (2021) 118–125.

[46] X. Liu, W. Zhou, Y. Yang, K. Cheng, J. Kang, L. Zhang, G. Zhang, X. Min, Q. Zhang, Y. Wang, Design of efficient bifunctional catalysts for direct conversion of syngas into lower olefins via methanol/dimethyl ether intermediates, Chem. Sci. 9 (2018) 4708–4718.

[47] J. Mou, X. Fan, F. Liu, X. Wang, T. Zhao, P. Chen, Z. Li, C. Yang, J. Cao, CO_2 hydrogenation to lower olefins over Mn_2O_3-ZnO/SAPO-34 tandem catalysts, Chem. Eng. J. 421 (2021), 129978.